Electromechanical model of excitable tissue to study reentrant cardiac arrhythmias

Martyn P. Nash[a],*, Alexander V. Panfilov[b,c]

[a] *Bioengineering Institute and Department of Engineering Science, The University of Auckland, Private Bag 92019, Auckland, New Zealand*
[b] *Theoretical Biology, University of Utrecht, Padualaan 8, 3584 CH, Utrecht, The Netherlands*
[c] *Division of Mathematics, University of Dundee, Dundee DD1 4HN, UK*

Abstract

We introduce the concept of a contracting excitable medium that is capable of conducting non-linear waves of excitation that in turn initiate contraction. Furthermore, these kinematic deformations have a feedback effect on the excitation properties of the medium. Electrical characteristics resemble basic models of cardiac excitation that have been used to successfully study mechanisms of reentrant cardiac arrhythmias in electrophysiology. We present a computational framework that employs electromechanical and mechanoelectric feedback to couple a three-variable FitzHugh–Nagumo-type excitation-tension model to the non-linear stress equilibrium equations, which govern large deformation hyperelasticity. Numerically, the coupled electromechanical model combines a finite difference method approach to integrate the excitation equations, with a Galerkin finite element method to solve the equations governing tissue mechanics. We present example computations demonstrating various effects of contraction on stationary rotating spiral waves and spiral wave break. We show that tissue mechanics significantly contributes to the dynamics of electrical propagation, and that a coupled electromechanical approach should be pursued in future electrophysiological modelling studies.
© 2004 Elsevier Ltd. All rights reserved.

*Corresponding author. Tel.: +64-9373-7599x82550; fax: +64-9367-7157.
E-mail addresses: martyn.nash@auckland.ac.nz (M.P. Nash), A.V.Panfilov@bio.uu.nl (A.V. Panfilov).
URLs: http://www.esc.auckland.ac.nz/People/Staff/Nash/, http://www-binf.bio.uu.nl/~panfilov/.

1. Introduction

Sudden cardiac death is the main cause of mortality in the industrialised world (Pool, 1990) and many dangerous cardiac arrhythmias have been shown experimentally and theoretically to be driven by reentrant electrical sources (Allessie et al., 1973; Davidenko et al., 1992) or rotating spiral waves of excitation (Winfree, 1989; Davidenko et al., 1992; Pertsov et al., 1993). The various dynamics of reentrant spiral waves have been linked to the underlying class of cardiac arrhythmia. For example, stationary rotation of spiral waves has been associated with monomorphic tachycardia, non-stationary rotation (or drift) has demonstrated characteristics of polymorphic tachycardia and torsade de pointes, whilst the break up of spiral waves into complex spatio-temporal patterns has been linked with fibrillation (Abildskov and Lux, 1991; Gray et al., 1995; Garfinkel and Qu, 1999).

Sudden cardiac death during ventricular fibrillation (VF) results in compromised mechanical pump function of the heart. Cardiac contraction is initiated by electrical depolarisation, but turbulent patterns of excitation during VF result in desynchronised cardiac contractions. In general, this mechanoelectric feedback is a complex issue that has been studied in the clinical community for well over a century (see reviews in Kohl and Ravens, 2003), and may have both pro-rhythmic and arrhythmogenic consequences. For example, mechanical deformation has been shown to alter the electrical properties of myocytes (Sigurdson et al., 1992) and play an important role in ventricular arrhythmias (Franz et al., 1992).

Mathematical modelling is a useful technique for investigating the electrical activity of the heart, and several mechanisms of cardiac fibrillation have been proposed on the basis of modelling studies (Moe et al., 1964; Panfilov and Pertsov, 2001). Modelling has also been used to study the spatio-temporal dynamics of reentrant arrhythmias in 2D, 3D, and in anatomically accurate models of the heart (see articles in Christini and Glass, 2002). Present models of electrical activity of the heart are capable of reproducing a variety of experimental observations, and biophysics of these models has been based on data from sound electrophysiological experiments. The detail, complexity and predictive capability of these models have evolved over the past 40 years. The first computations of reentrant activity started in 1972 (Gul'ko and Petrov, 1972), and progressed thereafter from simple two-variable models of excitable media, to the modern biophysical models of cardiac tissue. Interestingly, the success of many predictions was based on observations first encountered using simple models. For example, basic effects such as the structure of the spiral wave core (Panfilov and Pertsov, 1981), meandering of spiral waves in 2D (Zykov, 1987), curvature-induced filament drift in 3D (Panfilov and Pertsov, 1984), etc., were first predicted by basic models of excitable media and subsequently extended to the more detailed biophysical model descriptions.

None of the studies cited above, even the most detailed, have accounted for the active mechanical contraction of the heart, nor even the basic effects of deformation on reentrant arrhythmias. A variety of computational models have been used to investigate the effects of electrical activity on the sequence of 3D ventricular contraction (Guccione et al., 1995; Nash and Hunter, 2000; Usyk et al., 2002; Kerckhoffs et al., 2003), but these models have not accounted for the effects of mechanoelectric feedback. On the other hand, detailed modelling studies of the effects of mechanics on cardiac electrophysiology (such as Vetter and McCulloch, 2001) have not accounted for effects of excitation–contraction coupling. One study has combined

electromechanical and mechanoelectric feedback modelling (Hunter et al., 1997) and whilst the continuum framework was presented in detail, the report contained limited interpretation of the results.

The aim of this study was to establish a computational framework to study the combined effects of cardiac mechanics and the dynamics of electrical activity during arrhythmia. We begin with the most basic description of a coupled electromechanical model (for which many of the biological details are absent), then systematically incorporate the effects of mechanoelectric feedback. In this article, we discuss the general aspects of electromechanical and mechanoelectric feedback modelling and propose a fully coupled model of contracting excitable tissue. We illustrate the applicability of the computational electromechanical framework to study reentrant sources of excitation in the form of 2D spiral waves in normal and turbulent regimes.

2. Cardiac excitation modelling

Cardiac contraction is initiated by propagating electrical waves of excitation. The spread of excitation in the heart occurs due to excitability of individual cardiac cells and due to close electrical coupling of cardiac cells via specialised contacts (gap junctions), through which depolarised cardiac cells can elicit excitation in neighbouring cells, resulting in a propagation wave of activity. Thus, models that describe propagation in the heart generally consist of two parts: a model of the cardiac cell, and a model describing cellular interconnections.

In general terms, excitation of a cardiac cell is brought about by the change in potential across the cell membrane, due to transmembrane fluxes of various charged ions (Na^+, K^+, Ca^{2+}, Cl^-, etc.). A mathematical description of these processes is based on the following equation (Keener, 1998):

$$I = C_m \frac{dV}{dt} + I_m, \tag{1}$$

where I represents the total transmembrane current, C_m is the membrane capacitance, V is the transmembrane potential, and I_m is the total ionic transmembrane current, which will be discussed later.

To describe the time course of excitation of a single cardiac cell in the absence of external currents, one can solve Eq. (1) with $I = 0$. To describe wave propagation in cardiac tissue, it is necessary to specify the currents resulting from the intercellular coupling, which can usually be approximated using (Keener, 1998):

$$I = \nabla \cdot (\mathbf{D} \nabla V) = C_m \frac{\partial V}{\partial t} + I_m, \tag{2}$$

where $\mathbf{D}$ is a tensor of conductivities, and ∇ is the one-, two-, or three-dimensional gradient operator.

Taken together with appropriate descriptions of the transmembrane ionic currents (I_m), Eq. (2) constitutes a model for the electrical properties of cardiac tissue.

2.1. Ionic and FitzHugh–Nagumo models for cardiac cells

There are two classes of mathematical descriptions for I_m. *Biophysical* or *ionic* models are based on direct experimental observations derived from voltage clamp and patch clamp studies, and generally include many Hodgkin–Huxley type equations to describe individual ionic currents that cross the cell membrane (Hodgkin and Huxley, 1952; Noble, 1962). Modern ionic models also describe the changes of concentrations of all major ions inside cardiac cells, and generally consist of anywhere between 10 and 60 ODEs (Luo and Rudy, 1994; Noble et al., 1998). The quantitative descriptions of ionic currents in cardiac tissue are continually being revised, and although they can accurately reproduce various properties of the cardiac action potential, such as shape, rate dependence, etc., there is not yet general agreement on the best model for all circumstances.

On the other hand, I_m can be described reasonably well using a phenomenological approach, based on simple two-variable FitzHugh–Nagumo (FHN)-type models (FitzHugh, 1961). These descriptions can reproduce macroscopic characteristics of cardiac tissue such as refractoriness, dispersion relation, simple rate duration properties, etc. The main advantage of these models is their simplicity and ability to explain basic properties of cardiac tissue. FHN-type models can be customised to quantitatively reproduce certain overall characteristics of cardiac tissue important for propagation, such as restitution of action potential duration (Kogan et al., 1991; Aliev and Panfilov, 1996; Fenton and Karma, 1998) and restitution of conduction velocity. (Fenton and Karma, 1998).

The choice of the description for I_m (ionic versus FHN-type model) is typically made in the context of the type problem to be investigated. Studies of various effects of drug application, gene expressions, etc., on the shape of the action potential requires the use of ionic models, because the ion channel proteins modified by these interventions are not individually accounted for in the FHN-type models. On the other hand, if one studies propagation and particularly arrhythmias in cardiac tissue, then a detailed description of the shape of the action potential is generally not essential. The more important factors affecting the propagation are the macroscopic properties of cardiac tissue, such as velocity of the excitation wave, restitution properties, etc. Thus, for cardiac propagation and its relation to the overall properties of cardiac tissue, it can be more effective to use FHN-type models, which have been customised using appropriate experimental data. Furthermore, phenomena predicted by FHN-type models have often been confirmed using biophysical models of cardiac tissue (Winfree, 1989).

In this study, we investigated the basic effects of cardiac contraction on 2D reentrant spiral wave activity, without concern for the details of the individual ionic currents. For this reason, we chose to use a simple FHN approach, as described in Section 2.2.

2.2. Aliev–Panfilov modifications to the FitzHugh–Nagumo model

Aliev and Panfilov (1996) proposed the following two variable model of cardiac tissue:

$$\frac{\partial V}{\partial t} = \nabla \cdot (\mathbf{D}\nabla V) - kV(V - a)(V - 1) - rV + I_s, \tag{3}$$

$$\frac{\partial r}{\partial t} = \left(\varepsilon + \frac{\mu_1 r}{\mu_2 + V}\right)(-r - kV(V - b - 1)), \tag{4}$$

where V is a dimensionless representation of the transmembrane potential, r is a dimensionless representation of the conductance of a slow inward (repolarising) current, t is a dimensionless time variable, and I_s is the current due to an external stimulus. Note that all of the terms in Eqs. (3) and (4), including the temporal and spatial derivatives are non-dimensional (discussed further below) and the capacitance is implicitly included.

The term $-kV(V-a)(V-1)$ in Eq. (3) controls the fast processes, such as the initiation and upstroke of the action potential. Dynamics of the recovery phase and restitution properties of the action potential are determined by the time course of r, which is primarily controlled by the term $(\varepsilon + (\mu_1 r)/(\mu_2 + V))$. Apart from the threshold parameter, a, the parameters of this model (k, μ_1, μ_2, b) do not have clear physiological meanings, but are adjusted to reproduce key characteristics of cardiac tissue, such as the shape of the action potential, refractoriness and restitution of action potential duration.

Although FHN-type models use dimensionless units, simulation results are often compared to dimensional observations from experimental studies. To this end, dimensional mappings are usually determined by comparing specific (dimensionless) model characteristics with experimental observations. For example, the action potential duration (APD) computed using the Aliev and Panfilov (1996) model was 25.58 dimensionless time units, whilst Elharrar and Surawicz (1983) measured a canine cardiac APD of 330 ms. Based on these data, Aliev and Panfilov (1996) scaled their dimensionless temporal results by 12.9 ms for physiological comparison. Another frequently used scaling method is based on the comparison of a spiral wave period for a given model with a characteristic period of cardiac arrhythmia (Panfilov, 1998). In order to produce dimensioned values for length units, one can compare model and experimental data for the velocity of wave propagation (Winfree, 1989), or spiral wavelengths (Panfilov, 1998). Similarly, dimensional transmembrane voltages can be obtained by mapping the dimensionless variable V, which ranges over the interval [0,1], onto a dimensioned interval determined from an experimental study. For example, Elharrar and Surawicz (1983) recorded the resting potential (-80 mV) and action potential amplitude (100 mV) in the dog heart. Accordingly, Aliev and Panfilov (1996) mapped V onto this physiological interval (-80 mV, 20 mV) using the obvious linear scaling $E[mV] = -80 + 100V$.

In comparison to the original FitzHugh (1961) model, the Aliev and Panfilov (1996) model provides a more realistic shape of the cardiac action potential, since the hyper-repolarisation overshoot is eliminated. The parameters of the latter model have also been customised to reproduce the APD restitution characteristics observed in the canine ventricle (Elharrar and Surawicz, 1983), as illustrated in Fig. 1.

The Aliev and Panfilov (1996) model has been used to study different types of propagation in 2D and 3D cardiac tissue, and in anatomically accurate models of the heart (Gray and Jalife, 1998; Panfilov, 1999a, b, 2002). The model reproduces most of the regimes important for understanding reentrant activity, such as stationary rotation of spiral waves, meandering of spiral waves and spiral wave break up. In this paper, we have extended the Aliev and Panfilov (1996) model to include an approximation of the actively developed stress during contraction to investigate the effects of mechanical deformation on cardiac excitation and various types of reentrant activity.
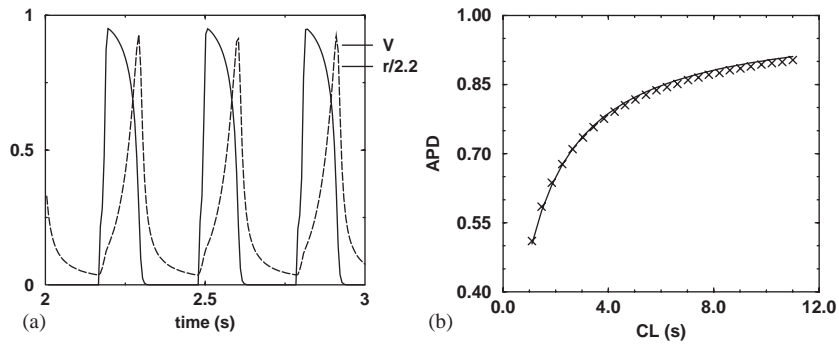
Fig. 1. Properties of action potential described by the Aliev and Panfilov (1996) model. (a) Time course of excitation (*V*) and recovery (*r*; scaled for clarity) variables during stimulation at a period of 312 ms. (b) Normalised (dimensionless) action potential duration (APD) restitution as a function of cycle length (CL) of the model (solid line) compared to experimental observations (crosses) from canine myocardium (Elharrar and Surawicz, 1983).

3. Modelling cardiac tissue mechanics

Cardiac cells change length by up to 20% during a normal heart beat, so mechanical analysis must be based on finite deformation elasticity theory. Here we present summaries of the kinematics of large deformation, stress equilibrium, and the finite element basis functions which extend the analysis to non-regular geometries. For more detailed explanations of the theory, the reader is referred to more comprehensive publications cited throughout this section. Simple constitutive laws for passive and active material response are then described, together with isotonic boundary loading conditions used in this study.

3.1. Kinematics and stress

Let $\mathbf{x} = \{x_i\}$ denote the present (deformed) position in rectangular cartesian coordinates of a material particle that occupied the location $\mathbf{X} = \{X_M\}$ in the reference (undeformed) configuration. In standard finite deformation theory, $\mathbf{X}$ may be considered as material (or convected) coordinates and the deformation gradient tensor, $\mathbf{F}$, transforms the undeformed material line segment, $d\mathbf{X}$, into the deformed line segment defined by $d\mathbf{x} = \mathbf{F}\,d\mathbf{X}$. In component form, $dx^i = F_M^i\,dX^M$, where the components of the deformation gradient tensor are defined by

$$F_M^i = \frac{\partial x_i}{\partial X_M}. \tag{5}$$

Polar decomposition splits $\mathbf{F} = \mathbf{RU}$ into the product of an orthogonal rotation tensor, $\mathbf{R}$, and a symmetric positive definite stretch tensor, $\mathbf{U}$, which contains a complete description of the material strain, independent of any rigid-body motion (Atkin and Fox, 1980, Section 1.4). The right Cauchy–Green deformation tensor, $\mathbf{C} = \mathbf{U}^2$ (Atkin and Fox, 1980, p. 12), and Lagrangian Green's strain tensor, $\mathbf{E}$ (Spencer, 1980, p. 72) are defined by

$$\mathbf{C} = \mathbf{F}^{\mathrm{T}}\mathbf{F} \quad \text{or} \quad C_{MN} = \left\{ \frac{\partial x_k}{\partial X_M} \frac{\partial x_k}{\partial X_N} \right\}, \tag{6}$$

$$\mathbf{E} = \tfrac{1}{2}(\mathbf{C} - \mathbf{I}), \tag{7}$$

where $\mathbf{I}$ is the identity matrix. Note that $\mathbf{C}$ and $\mathbf{E}$ are symmetric tensors by definition.

The principal invariants of the right Cauchy–Green deformation tensor are defined by

$$I_1 = \operatorname{tr}\mathbf{C}, \quad I_2 = \tfrac{1}{2}[(\operatorname{tr}\mathbf{C})^2 - \operatorname{tr}\mathbf{C}^2], \quad I_3 = \det\mathbf{C}, \tag{8}$$

where the trace of $\mathbf{C}$, denoted by $\operatorname{tr}\mathbf{C}$, is the sum of the diagonal terms, and $\det\mathbf{C}$ denotes the determinant of $\mathbf{C}$ (Atkin and Fox, 1980, Section 1.4). These are useful for describing isotropic constitutive behaviour as outlined in Section 3.4. The next step is to develop the stress equilibrium equations that govern finite deformation elasticity.

3.2. Stress equilibrium

To represent material behaviour independent of rigid-body motion, it is convenient to define the state of mechanical stress of the tissue in terms of the second Piola–Kirchhoff tensor, T^{MN} (Malvern, 1969, p. 220), which represents the force per unit undeformed area, acting on an infinitesimal element of surface in the reference configuration. Second Piola–Kirchhoff stress components can be defined solely in terms of material coordinates, just as for the Green's strain tensor (Eq. (7)). Conservation of angular momentum restricts the second Piola–Kirchhoff stress tensor to be symmetric for non-polar materials (Spencer, 1980, Section 7.5).

The equations that govern finite deformation elasticity arise from the conservation of linear momentum following Newton's laws of motion (Malvern, 1969, Section 5.3). For static equilibrium in the absence of body forces, the governing equations expressed in terms of second Piola–Kirchhoff stress components reduce to

$$\frac{\partial}{\partial X_M}(T^{MN}F_N^j) = 0. \tag{9}$$

By introducing a weighting field of virtual displacements, $\delta\mathbf{v} = \{\delta v_j\}$, the weak form of the stress equilibrium equations can be written as

$$\int_{V_0} T^{MN}F_N^j\frac{\partial(\delta v_j)}{\partial X_M}\,\mathrm{d}V_0 = \int_{S_2} \mathbf{s}\cdot\delta\mathbf{v}\,\mathrm{d}S, \tag{10}$$

where V_0 is the undeformed volume and S_2 is the portion of the boundary subject to external tractions, $\mathbf{s}$. Note that these equations may be formally derived via the principle of virtual work (Malvern, 1969, Section 5.5).

3.3. Finite element approximations

For finite element analysis of mechanics problems, it is convenient to approximate the undeformed and deformed geometric coordinates ($\{X_M\}$ and $\{x_i\}$, respectively) using a finite element interpolation scheme. Element coordinates $\{\xi_k\}$ are normalised material coordinates that move with the deforming body and provide the parameterisation of the geometric variables within an element:

$$X_M = \Psi_n(\{\xi_k\})X_M^n, \tag{11}$$

$$x_i = \Psi_n(\{\xi_k\})x_i^n, \tag{12}$$

where $\Psi_n(\{\xi_k\})$ are the interpolation functions (chosen to be bilinear for this study), and X_M^n and x_i^n represent the undeformed and deformed geometric variables, respectively, defined at finite element nodes (n).

Using the same interpolation functions, the virtual displacement fields $\{\delta v_j\}$ in Eq. (10) can be approximated using

$$\delta v_j = \Psi_n(\{\xi_k\})\delta v_j^n, \tag{13}$$

where δv_j^n are virtual nodal displacements. Substituting Eq. (13) into the stress equilibrium equations (Eq. (10)) and setting the coefficient of each arbitrary displacement component δv_j^n to zero, gives

$$\int_{V_0} T^{MN} F_N^j \frac{\partial \Psi_n}{\partial X_M} \, dV_0 = f_n^j, \tag{14}$$

where f_n^j are the external nodal traction forces (discussed in Section 3.5).

Eq. (14) represents the set of global residual equations arising from the finite element model. Note that there are $j*n$ residuals: one for each geometric coordinate (j) at each finite element node (n) of the model.

To solve the global equations, the domain integrals in Eq. (14) are replaced by a sum of integrals over a non-overlapping collection of undeformed element domains that constitute the finite element model. For evaluation purposes, element integrals are transformed from the spatial reference coordinates to the ξ_k-coordinate space, yielding

$$\int\int_0^1\int T^{MN} F_N^j \frac{\partial \Psi_n}{\partial \xi_k} \frac{\partial \xi_k}{\partial X_M} J \, d\xi_1 \, d\xi_2 \, d\xi_3 = 0, \tag{15}$$

where the Jacobian of the coordinate transformation is defined by

$$J = \left| \frac{\partial \xi_p}{\partial X_Q} \right|. \tag{16}$$

Eq. (15) if the starting point for a computational implementation of the finite element method for large deformation mechanics. These element integrals can be evaluated using Gaussian quadrature, then assembled to construct the set of global residual equations (Eq. (14)).

Given the undeformed model geometry, mechanical properties and boundary loads (considered in the next sections), the unknowns of the problem are the deformed geometric coordinates, which can be determined using Newton's method to minimise the non-linear residual equations (Eq. (14)). This iterative solution process requires an initial estimate of the deformed coordinates. A useful estimate is the undeformed geometry, modified by any incremental displacement boundary conditions. For a given estimated solution, all of the terms in Eq. (15) can be evaluated at any point in the domain (such as the Gaussian quadrature points). In particular, the deformation gradient components (F_N^j) can be directly determined from the geometric variables and interpolation functions, and the components of the second Piola–Kirchhoff stress tensor (T^{MN}) can be evaluated using the constitutive equations described in Section 3.4.

3.4. Mechanical properties of passive tissue

The purpose of a constitutive law is to express, as succinctly as possible, the experimentally observed relationship between a material's stress and strain tensors over the range of stress or strain likely to be encountered in the application of the law. It is essential that constitutive laws are based on experiments using real materials, but certain theoretical restrictions must be observed.

Firstly, constitutive equations must be independent of the choice of coordinate system, since they characterise the constitution of individual materials, but not the frame of reference from which they are observed. Thus rigid-body motions play no role in the constitutive law (this is known as the *axiom of objectivity*, see Eringen, 1980, p. 163). This can be satisfied by postulating the existence of a scalar strain energy density function, W, that depends on the components of the right Cauchy–Green deformation tensor (Eq. (6)).

Components of the second Piola–Kirchhoff stress tensor are given by the derivatives of W, as defined in Eq. (17) (Green and Adkins, 1970, p. 6).

$$T^{MN} = \frac{1}{2}\left(\frac{\partial W}{\partial E_{MN}} + \frac{\partial W}{\partial E_{NM}}\right), \tag{17}$$

where Green's strain components (E_{MN}) are referred to X_M-material coordinates.

Material symmetry imposes further theoretical restrictions on the form of the constitutive law. For *isotropic* materials, which exhibit identical mechanical properties in all directions, a suitable functional form of W is (Spencer, 1980, Section 10.2)

$$W(I_1, I_2) = c_1(I_1 - 3) + c_2(I_2 - 3), \tag{18}$$

which gives a good fit for certain types of soft rubbers and silicone gels, known as *Mooney–Rivlin* materials. I_1, I_2 are defined in Eq. (8), and c_1 and c_2 are the material constants with units of stress (kPa). Note that the use of (I_1-3) and (I_2-3) ensures that the strain energy is zero when the strain is zero.

Experimental evidence has shown that cardiac tissue exhibits different response along the various material axes (Smaill and Hunter, 1991; Dokos et al., 2002) and this has important implications for both cardiac mechanics (Nash and Hunter, 2000) and electrical activation in myocardial tissue (see reviews in Kohl and Ravens, 2003). However, the added complexities due to this anisotropic behaviour have been neglected in this study (anisotropy will be considered in future studies). Instead, isotropic, homogeneous passive material properties have been assumed ($c_1 = 2$ kPa and $c_2 = 6$ kPa) in order to more easily understand the direct effects of contraction on the electrical activity.

3.5. Uniform isotonic boundary loads

Two main types of boundary conditions are commonly used to constrain mechanics models:

- *Geometric constraints*: Nodal coordinates are fixed to predetermined deformed values. Each constraint of this type eliminates one degree of freedom and thus one equation from the global system.

- *Point forces*: External tractions are applied at nodes of the finite element mesh. These constraints effectively add right-hand-side terms to the global equations, but do not reduce the size of the system.

A uniform load acting perpendicular to a surface (or edge for 2D models) can be applied to external boundaries by calculating equivalent nodal forces based on the geometric interpolation scheme. For example, a uniform load p kN m^{-1} applied to the edge of a 2D element may be equivalently represented by a vector of traction forces with components:

$$f_n^j = \int_{s_2} p \Psi_n n_j \, \mathrm{d}s, \tag{19}$$

where Ψ_n are the geometric interpolation functions, n_j are the coordinates of a vector normal to the boundary, s is an arc-length coordinate, and the integral is evaluated over the loaded edge s_2. If the load p is applied to an edge of length L of a 2D bilinear element, then the contribution to the global load vector is $pL/2$ for each of the two nodes adjacent to the loaded edge. Furthermore, a global node shared by two elements that are each subject to p will receive load contributions from both elements.

For the 2D models used in this study, a uniform isotonic load of 10 kN m^{-1} was applied to the external edges of the excitable medium. In addition, the central node of the model was completely fixed in space to prevent rigid-body translations, and the first geometric coordinate of an adjacent node was fixed to prevent rigid body rotations.

4. Electromechanical and mechanoelectric feedback modelling of cardiac tissue

In order to mathematically couple the electrical and mechanical activity of the heart, the relationships between the equations of electrical activity (Eq. (2)) and cardiac mechanics (Eq. (9)) must be considered.

The effects of mechanical activity on cardiac excitation are complex and not completely understood. In general, each of the constitutive properties in Eq. (2) may depend on the state of deformation, resulting in

$$\nabla \cdot (\mathbf{D}(\mathbf{C})\nabla V) = C_{\mathrm{m}}(\mathbf{C})\frac{\partial V}{\partial t} + I_{\mathrm{m}}(\mathbf{C}), \tag{20}$$

where $\mathbf{C}$ is the Cauchy–Green deformation tensor, defined in Eq. (6).

Eq. (20) illustrates the dependence of the passive electrical properties of cardiac tissue, namely the conduction tensor $\mathbf{D}$ and the membrane capacitance C_{m}, on the deformation tensor $\mathbf{C}$ (Dominguez and Fozzard, 1979). Deformation also influences excitation via stretch-activated channels (a component of I_{m}), which can dramatically change the shape of action potential in response to stretch (see the review by Kohl et al., 1999). Another direct influence of conduction on excitation is that the operator $\nabla \cdot (\mathbf{D}(\mathbf{C})\nabla V)$ should be evaluated in a general curvilinear coordinate system, which can be determined from the deformation tensor.

Modelling the effects of excitation on contraction requires a detailed knowledge of the active stresses generated by myocytes as they depolarise. In normal cardiac tissue, the active components of stress depend on the intracellular concentration of calcium ions $[Ca^{2+}]_i$, the history of sarcomere length changes, and a range of other factors such as the kinetics of calcium binding to troponin C (Hunter et al., 1998). In a modelling context, active and passive (second Piola–Kirchhoff) stress components are linearly superimposed to define the total state of stress of the tissue (Hunter et al., 1997).

In this study, we have also superimposed the passive and active stress components, but have not attempted to quantify the biophysical details of electromechanical coupling, nor the anisotropic mechanical behaviour of cardiac tissue. Instead, we have used a single ODE to approximate the active contractile stress, and have assumed that active stresses are directly dependent on the transmembrane potential, and are spatially isotropic. To this end, the Aliev and Panfilov (1996) model has been modified to introduce a new variable T_a to represent the active stress (defined below). We then define the mechanical material properties of the tissue using

$$T^{MN} = \frac{1}{2}\left(\frac{\partial W}{\partial E_{MN}} + \frac{\partial W}{\partial E_{NM}}\right) + T_a C^{MN}, \tag{21}$$

where C^{MN} are components of the contravariant metric tensor, which can be computed from the covariant metric tensor (Eq. (6)) using $\{C^{MN}\} = \{C_{MN}\}^{-1}$ since the undeformed material coordinates are orthogonal.

In this study, we have neglected the capacitive and ionic dependencies on contraction, and have simply focussed on the effects of tissue deformation on conduction, as described by the first term in Eq. (20). By expressing the gradients with respect to the material coordinate system, the equations for electrical activity can be written as:

$$C_m \frac{\partial V}{\partial t} = \frac{1}{\sqrt{C}} \frac{\partial}{\partial X^M}\left(\sqrt{C} D_N^M C^{NL} \frac{\partial V}{\partial X^L}\right) - kV(V-a)(V-1) - rV + I_s, \tag{22a}$$

$$\frac{\partial r}{\partial t} = \left(\varepsilon + \frac{\mu_1 r}{\mu_2 + V}\right)(-r - kV(V - b - 1)), \tag{22b}$$

$$\frac{\partial T_a}{\partial t} = \epsilon(V)(k_{T_a} V - T_a), \tag{22c}$$

where $C = \det(\{C_{NL}\})$, k_{T_a} controls the amplitude of the active stress twitch, and the function $\epsilon(V)$ is defined by

$$\epsilon(V) = \begin{cases} \epsilon_0 & \text{for } V < 0.05, \\ 10\epsilon_0 & \text{for } V \geq 0.05 \end{cases} \tag{23}$$

with $\epsilon_0 = 1$. This function controls the delay in the development ($V < 0.05$) and recovery ($V \geq 0.05$) of active stress with respect to the action potential. Similar to many of the FHN-type models, we have assumed that $C_m = 1$ (dimensionless).

To integrate Eq. (22a), the spatial derivatives have been expanded using

$$\frac{1}{\sqrt{C}}\frac{\partial}{\partial X^M}\left(\sqrt{C}C^{ML}\frac{\partial V}{\partial X^L}\right) = C^{ML}\left(\frac{\partial^2 V}{\partial X^M\partial X^L} - \Gamma^N_{ML}\frac{\partial V}{\partial X^N}\right), \tag{24}$$

where Γ^N_{ML} are components of the Riemann–Christoffel tensor (Flugge, 1972).

The coupled electromechanical model is solved using a hybrid approach that incorporates finite difference methods to solve the electrical excitation problem, and non-homogeneous finite element techniques to compute the finite deformation mechanics of the tissue.

All derivatives in Eq. (22) are evaluated using finite difference approximations and the explicit Euler method is employed as the time integration scheme. Following a specified number of time integration steps (a parameter of the solution scheme, typically 80), the computed values of T_a from finite difference grid points are interpolated at finite element Gauss points. These active Gauss point stresses serve as inputs to load the tissue mechanics model. Non-linear Newton iterations are then performed to solve the stress equilibrium equations that govern mechanics, following which deformation tensors are updated and used to control the electrical conduction properties in Eq. (22a).

In this study, we considered isotropic conduction $D^M_N = \delta^M_N$ (the unitary tensor; dimensionless). Computations were performed using a time integration step of $\Delta t = 0.02$ (dimensionless) and a space integration step of $\Delta x = \Delta y = 0.6$ (dimensionless), consistent with previous studies (Panfilov, 2002). Mesh sizes of up to 251×251 grid points were used for the electrical problem, for which no-flux boundary conditions were imposed. To generate the initial reentrant wave, we used initial data corresponding to a broken wave front, with the break located at the middle of the excitable medium.

Although our activation model (Eq. (22)) is expressed in dimensionless units, we have illustrated temporal simulation results using dimensioned time units for further comparison with experimental data. To scale our dimensionless time variable, we followed the approach of Panfilov (1998), and set the period of a spiral wave (26.9 dimensionless units, using our parameter set) to 269 ms, which is within the limits of spiral wave periods predicted by detailed ionic models of cardiac tissue (Bernus et al., 2002, 2003). Thus the actual time integration step was 0.2 ms. Note that the other terms in Eq. (22) were kept dimensionless, because we did not intend to compare absolute values of transmembrane potential nor spatial characteristics.

A summary of the electromechanical model parameters is given in Table 1.

Table 1
Parameters for the coupled electromechanical model

Excitation parameters	$a = 0.1$	$k = 8.0$	$\mu_1 = 0.12$
	$\mu_2 = 0.3$	$C_m = 1$	$\varepsilon = 0.01$
	$k_{T_a} = 47.9\,\text{kPa}$	$\epsilon_0 = 1$	
FDM parameters	$\Delta t = 0.02$	$\Delta x = \Delta y = 0.6$	Up to 251×251 points
Mechanics parameters	$c_1 = 2\,\text{kPa}$	$c_2 = 6\,\text{kPa}$	$p_{\text{bdy}} = 10\,\text{kN}\,\text{m}^{-1}$
FEM parameters	Up to 25×25 elements	Bilinear interpolation	

Any variations on these parameters for the various models in this study are explicitly indicated in the text. FDM: finite difference method (excitation model); FEM: finite element method (mechanics model).

5. Results

The coupled electromechanical model described by Eqs. (14) and (22) was subjected to a uniform stimulation of period of 330 ms. The resulting electrical activity, active stresses and mechanical shortening of the excitable medium is illustrated in Fig. 2a. For the given mechanical material properties and boundary conditions, the parameters for the active stress ODE (k_{T_a} and ϵ_0 in Table 1) were adjusted to produce a maximal shortening of approximately 25%. With these parameters, peak shortening was delayed with respect to the peak of the action potential (V), but coincided with the maximal tension. Fig. 2b shows the dynamic APD restitution curve at 90% of repolarisation obtained using periodical stimulation of the excitable medium. These characteristics qualitatively resemble those of myocardial tissue. We have used this model of a contracting excitable medium to study the basic effects of contraction on 2D wave patterns.

All results presented in this study are in terms of the dimensionless potential V. To reproduce a physiologically realistic resting potential (-80 mV), and amplitude (100 mV) of the canine cardiac action potential (Elharrar and Surawicz, 1983), the dimensionless variable V in Fig. 2 can be scaled using $E[mV] = -80 + 100V$.

5.1. Point stimulus versus spiral wave excitation

Electromechanical activity due to a periodic point stimulation at the centre of the excitable medium is illustrated in Fig. 3. The resulting radially propagating waves of excitation elicited deformations that were symmetric about the central axes. Fig. 4 shows a similar model with a spiral wave rotating around the centre of the excitable medium. In this case, the deformations were non-symmetric, but were dependent on the phase of the spiral wave rotation.

The main effect of mechanical contraction was to introduce regional variation of deformation. In order to characterise local deformations, we quantified the mean change in area of a row of mechanical elements located along a horizontal line passing through the centre of the medium, and compared this to the mean area change for a horizontal row of elements at the lower boundary. These regional comparisons were done for the two stimulation protocols presented in Figs. 3 and 4. Note that for radial stimulation (Fig. 5a) the deformations at the boundary and at
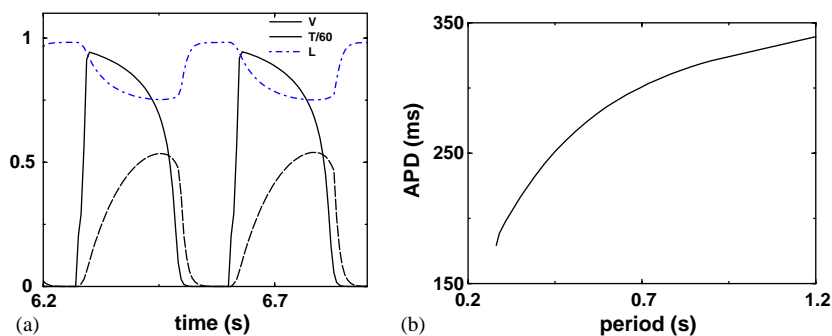

Fig. 2. (a) Action potential (V), relative shortening (L) and active stress (T; scaled for graphical clarity) variables as functions of time during uniform stimulation of the medium at a period of 330 ms. (b) The dynamic APD$_{90}$ restitution curve.
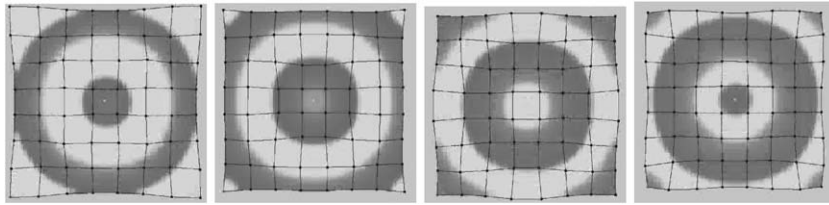
Fig. 3. A contracting excitable medium (described by Eq. (22)) subject to a central point stimulus with period of 310 ms and illustrated after 15 s of stimulation. Dark shading represents regions where $V > 0.6$. Lines depict boundaries of the mechanics finite elements, which each contain 10×10 finite difference grid points for the electrical model. The time interval between frames is 90 ms.
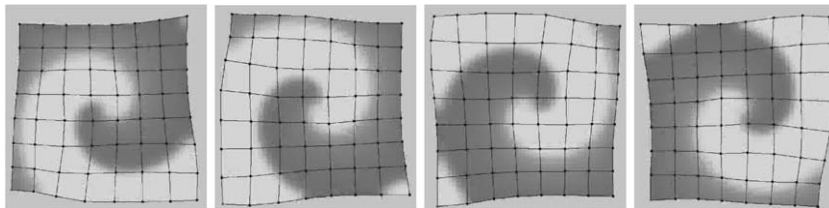

Fig. 4. Deformation of the excitable medium due to a centrally located spiral wave defined by Eq. (22) with $\mu_1 = 0.12$. The time interval between frames is 45 ms. The first frame is at time 15 s after initiation of the spiral wave.
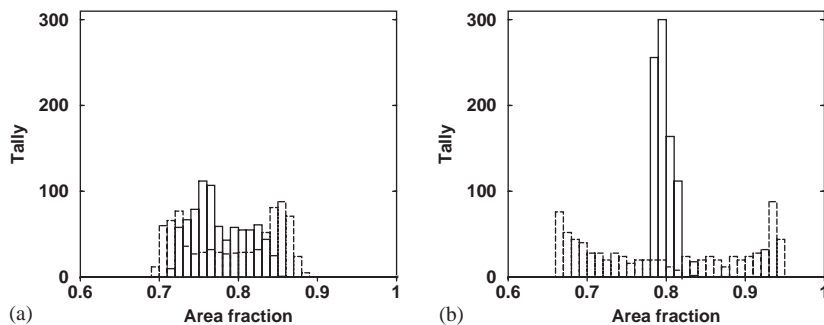
Fig. 5. Histograms of mean area fractions for a horizontal row of elements through the centre of the medium (solid bars), and a row of elements along the lower boundary of the medium (dashed bars) for (a) radial stimulation, and (b) spiral wave rotation. For each location, the mean area fraction of the 7 adjacent elements was sampled at 6 ms intervals during the period from 10 to 15 s.

the centre were similar. However, during spiral wave rotation (Fig. 5b) the boundary deformations showed a much wider variation than those for the centre of the medium, where the spiral core was located.

In order to characterise the global deformations of the medium for these two models, Fig. 6 illustrates the time-varying relative changes in area of the medium (compared to the resting configuration) for the results in Figs. 3 and 4. Note that spiral wave rotation is generally non-stationary (see below), thus in order to estimate the mechanical activity for the model in Fig. 4, the
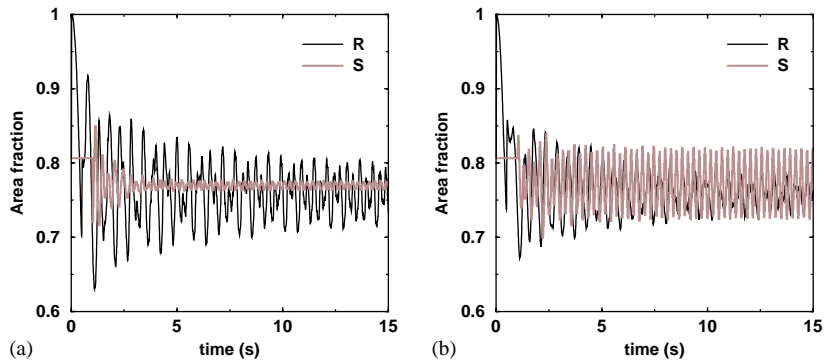
Fig. 6. The relative change in total medium area as a function of time during radial stimulation (R) and spiral wave rotation (S). The site of stimulation coincided with the location of the spiral core at (a) the centre of the medium; and (b) at a distance of 8 grid point spacings down and left of centre.

contraction–excitation feedback was temporarily removed from the equations (whilst of course maintaining the excitation–contraction coupling). As illustrated in Fig. 6a, the mechanical deformation caused by a centrally located rotating spiral wave was an order of magnitude less than that of the periodic radial waves. This difference was found to be due to the central location of the spiral wave. When the stimulation point and spiral wave core were shifted by 8 finite difference grid point spacings down and left of centre, the relative area changes were comparable (Fig. 6b).

5.2. Drift of the spiral wave

Next, the mechanoelectric feedback was reactivated and the spiral wave tip trajectories for the contracting and non-contracting excitable media were compared (Fig. 7). In the absence of contraction, the spiral wave core followed a stationary circular meander pattern (Fig. 7b). However, the dynamics of the spiral wave were drastically different for the contracting medium (Fig. 7d), for which the core meander was non-stationary. After approximately 30 reentrant rotations, the spiral tip trajectory had reached the boundary of the excitable medium, following which the core tracked around the edges. By the end of this computation (after approximately 50 rotations), the core had reached the upper left corner of the medium and continued to drift along the boundary, with no signs of becoming stationary (Fig. 7d). Note that when the spiral wave in the medium without contraction was artificially moved close to the boundary, it also drifted along the boundary (simulation results not shown), however the drift velocity was slower.

5.3. Reentrant wave periods

Spiral wave periods at four points in the contracting and non-contracting excitable media are compared in Fig. 8. In comparison to the non-contracting model, there was a much larger variation in spiral wave periods for the contracting medium. In addition, there was a small but significant increase in the mean spiral wave period during contraction (281 ± 29[SD] ms; $n = 144$
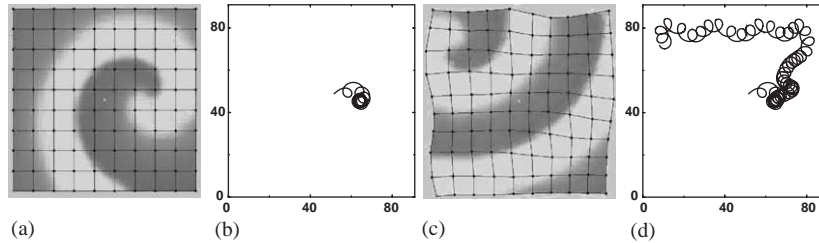
Fig. 7. Spiral wave rotation in (a,b) the absence, and (c,d) the presence of contraction. (a,c) illustrate wave patterns after 50 rotations from the two models subject to the same initial conditions. (b,d) show the spiral core tip trajectories for the entire computations.
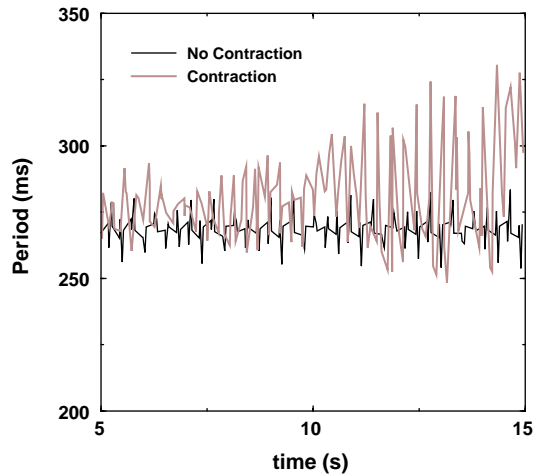

Fig. 8. Periods of spiral wave rotation for the contracting and non-contracting media.

periods quantified at 4 points over 36 wave rotations) in comparison to the non-contracting model (269 ± 3 ms; $n = 148$; at 4 points over 37 rotations; unpaired t-test $p < 0.01$).

5.4. Spiral wave break up

We next investigated the effects of contraction on the electrical activity during the process of spiral wave break up. In order to elicit wave break, the value of the parameter μ_1 in Eq. (22) was decreased, resulting in a steepening of the APD restitution curve from that shown in Fig. 1 (Panfilov, 2002). Wave patterns after 50 rotations for the contracting and non-contracting media are illustrated in Fig. 9. In both cases, the patterns of excitation have the qualitatively similar characteristic of being somewhat disorganised.

We attempted to characterise the patterns of excitation for these models, but comparison of two turbulent patterns is not trivial. Thus, just two basic characteristics were compared: the reentrant wave periods, and the numbers of electrical sources in the excitable media. Fig. 10a shows the periods measured at four different locations in the media to compare the contracting and
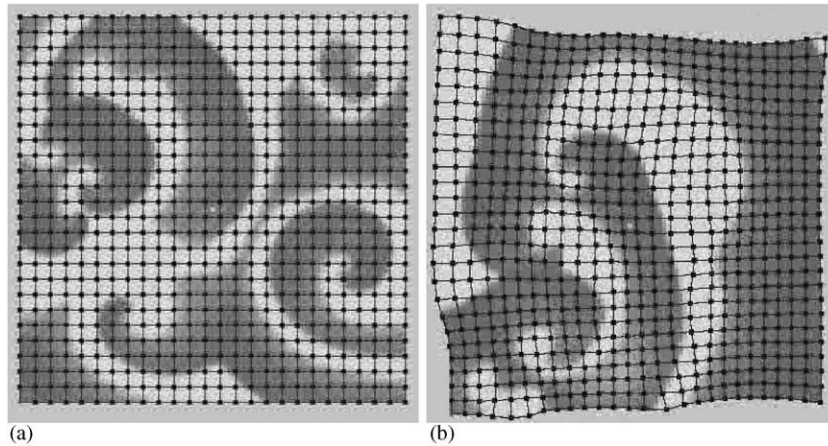
Fig. 9. Spiral wave break up in (a) non-contracting, and (b) contracting media consisting of a mesh of 25×25 mechanics elements and 251×251 electrical grid points. The same initial conditions were used for the two computations, which are illustrated after 50 rotations. To elicit wave break, both models used $\mu_1 = 0.07$ in Eq. (22).
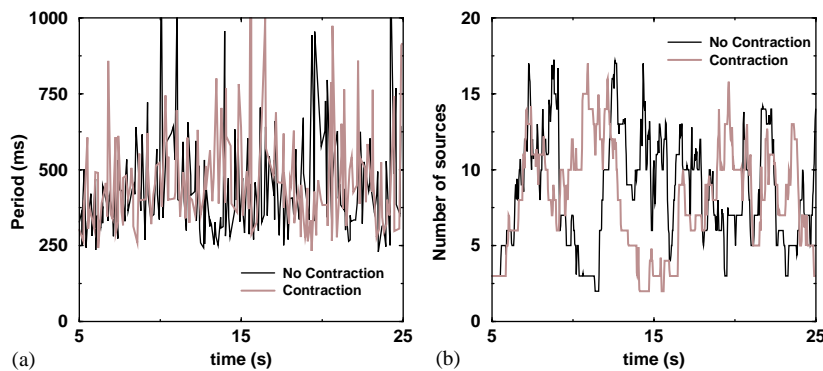

Fig. 10. Characteristics of spiral wave break up for the contracting and non-contracting media in Fig. 9. (a) Periods of excitation. (b) Number of reentrant sources.

non-contracting models. Dependencies were similar for both cases, although there was a small but significant increase in the period for the contracting medium (470 ± 170[SD] ms; $n = 196$ periods; quantified at 4 points over 49 rotations) in comparison to the non-contracting medium (440 ± 160 ms; $n = 208$ periods; 4 points over 52 rotations; unpaired t-test $p < 0.05$).

Another way to characterise the pattern of excitation following spiral wave break up is to count number of sources of excitation. (Fig. 10b) shows the time-varying number of sources for each model. Clearly, the dynamics of the excitation sources are complex, but the graphs for the two models appear qualitatively similar. However, statistical analysis showed a small but significant decrease in the mean number of sources for the contracting model (7.1 ± 4.0[SD]; $n = 15,987$) compared to the non-contracting model (7.4 ± 4.1; $n = 16,000$; unpaired t-test $p < 0.01$).
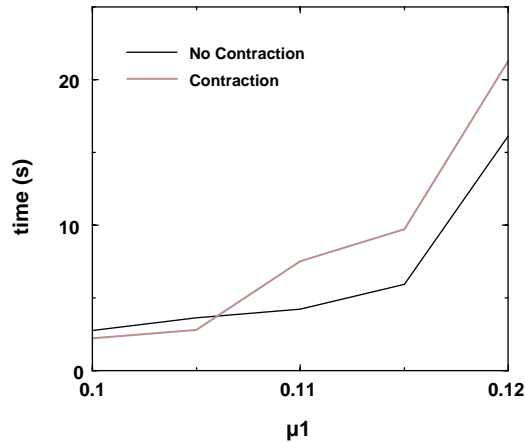
Fig. 11. Time of the first break up for contracting versus non-contracting media as a function of μ_1 in Eq. (22). Computations used models of 121×121 grid points, subject to identical initial conditions.

These results show that contraction slightly decreases the extent of spatio-temporal disorganisation by increasing the period of excitation and decreasing the number of sources present during the electrical turbulence.

Finally, we studied the effects of contraction on the initiation of spiral wave break up by quantifying the time of the first break up of a spiral wave as a function of the parameter μ_1 in Eq. (22). As illustrated in Fig. 11, the spiral wave break up occurred later for the contracting model compared to the non-contracting case (with all else being equal). This implies a damping effect of contraction on the process of spiral wave break up.

Under certain circumstances, motion of an excitable medium has been shown to induce the formation of new spiral waves. Biktashev et al. (1999) illustrated that an excitable medium moving with relative shear can initiate a 'chain reaction' of spiral wave births and deaths. Note, however, that in order to obtain this effect the shear motion of the medium was required to be persistent for several spiral wave rotations. Also, the velocity of the shearing motions was required to be comparable with the velocity of wave propagation in the medium, which is significantly less than deformations that occur during the cardiac cycle. Furthermore, the required shear motion is generally not persistent across any particular region of heart tissue. This mechanism could potentially play a role in the case of abrupt mechanical interventions on cardiac tissue. This also implies that the damping effect of contraction on spiral wave break up that we have observed is more likely to be due to mechanoelectric feedback as opposed to the motion of the excitable medium.

6. Conclusions and critique

In this study, a coupled electromechanical framework has been developed to investigate the effects of contraction on reentrant wave dynamics. The model is based on a three variable (voltage, inactivation and tension) description of the electrical activity, coupled to a model of

passive elasticity governed by the stress equilibrium equations, subject to an isotropic, Mooney–Rivlin material response and isotonic boundary loads. To illustrate the behaviour of the coupled electromechanical model, preliminary results suggest that mechanoelectric feedback could potentially cause an otherwise stationary spiral wave to meander about the medium. Furthermore, contraction possibly increases reentrant wave periods, whilst also increasing the extent of the period oscillations in the medium.

Note, however, that the effects found here should be considered as an indication of the importance of the mechanics for the spiral wave dynamics and not as firmly established results. Further research involving studies for different parameter values, numerical convergence, different boundary conditions and careful estimation of boundary effects is necessary to fully quantify these effects.

6.1. Limitations

The primary aim of the present study was to investigate the fundamental effects of contraction on wave propagation in excitable media. We did not intend to describe the biophysical mechanisms underlying excitation or contraction, thus the model has several essential limitations that should be addressed in future studies. The primary limiting assumptions of this study are listed here.

- Phenomenological model of cardiac excitation: the biophysics of specific ionic currents have not been considered.
- The effects of mechanics on the passive electrical properties of cardiac cells, and on ionic dynamics via the stretch activated ionic channels, have been neglected.
- Monodomain approximation: spatial gradients in the extracellular potential are assumed to be negligible. Thus the general bidomain equations have been reduced to the monodomain approach to excitation modelling, for which only the transmembrane potential field has been modelled.
- Simplified description of the passive mechanical properties of the medium (isotropic Mooney–Rivlin material response). It is clear that cardiac muscle exhibits anisotropic and non-homogeneous material properties, which have significant roles in controlling tissue deformation.
- Simplified isotropic active tension transient: active cell tension has been directly modelled using a single ODE dependent on the transmembrane potential. A more accurate description would define cell tension in terms of the voltage dependent intracellular calcium transient and changes in cell length, such as that described by Hunter et al. (1998). In addition, anisotropic active stresses, such as cross fibre tension, may play a significant role in electromechanical coupling.

Note that we did not intend to create a biophysically detailed quantitative model to study cardiac contraction. Rather, this research was focused on describing the possible effects of mechanics on excitation patterns, which must be verified using more physiologically realistic models.

6.2. Conclusions

The coupled electromechanical modelling presented here has demonstrated the potential for significant effects of contraction on the dynamics of reentrant electrical waves. Mechanical deformation can affect most of the basic properties of spiral waves, such as the period of excitation, stability of rotation of spiral waves, and the dynamics of development of spatio-temporal chaotic patterns and their characteristics. Therefore, modelling results and observations from static electrophysiological modelling studies should be interpreted with caution. Further research is needed to quantify the results illustrated in this study.

Acknowledgements

References

Abildskov, J.A., Lux, R.L., 1991. The mechanism of simulated Torsade de Pointes in a computer model of propagated excitation. J. Cardiovasc. Electrophysiol. 2, 224–237.

Aliev, R.R., Panfilov, A.V., 1996. A simple two-variable model of cardiac excitation. Chaos, Solitons and Fractals 7 (3), 293–301.

Allessie, M.A., Bonke, F.I.M., Schopman, F.J.G., 1973. Circus movement in rabbit atrial muscle as a mechanism of tachycardia. Circ. Res. 33, 54–62.

Atkin, R.J., Fox, N., 1980. An Introduction to the Theory of Elasticity. Longman Group Limited, London.

Bernus, O., Wilders, R., Zemlin, C.W., Verschelde, H., Panfilov, A.V., 2002. Computationally efficient electrophysiological model of human ventricular cells. Am. J. Physiol. 282 (6), H2296–H2308.

Bernus, O., Verschelde, H., Panfilov, A.V., 2003. Spiral wave stability in cardiac tissue with biphasic restitution. Phys. Rev. E 68, 021917.

Biktashev, V.N., Biktashev, I.V., Holden, A.V., Tsyganov, M.A., Brindley, J., Hill, N.A., 1999. Spatiotemporal irregularity in an excitable medium with shear flow. Phys. Rev. E 60, 1897–1900.

Christini, D.J., Glass, L. (Eds.), 2002. Mapping and control of complex cardiac arrhythmias. Chaos 12(3), 732–981.

Davidenko, J.M., Pertsov, A.M., Salomonsz, R., Baxter, W.T., Jalife, J., 1992. Stationary and drifting spiral waves of excitation in isolated cardiac muscle. Nature 355, 349–351.

Dokos, S., Smaill, B.H., Young, A.A., LeGrice, I.J., 2002. Shear properties of passive ventricular myocardium. Am. J. Physiol. 283, H2650–H2659.

Dominguez, G., Fozzard, H.A., 1979. Effect of stretch on conduction velocity and cable properties of cardiac Purkinje fibers. Am. J. Physiol. 6, C119–C124.

Elharrar, V., Surawicz, B., 1983. Cycle length effect on restitution of action potential duration in dog cardiac fibers. Am. J. Physiol. 244, H782–H792.

Eringen, A.C., 1980. Mechanics of Continua. Krieger, New York.

Fenton, F., Karma, A., 1998. Vortex dynamics in three-dimensional continuous myocardium with fiber rotation: filament instability and fibrillation. Chaos 8, 20–47.

FitzHugh, R.A., 1961. Impulses and physiological states in theoretical models of nerve membrane. Biophys. J. 1, 445–466.

Flugge, W., 1972. Tensor Analysis and Continuum Mechanics. Springer, New York.

Franz, M.R., Cima, R., Wang, D., Profitt, D., Kurz, R., 1992. Electrophysiological effects of myocardial stretch and mechanical determinants of stretch-activated arryhthmias. Circulation 86, 968–978.

Garfinkel, A., Qu, Z., 1999. Nonlinear dynamics of excitation and propagation in cardiac tissue. In: Zipes, D.P., Jalife, J. (Eds.), Cardiac Electrophysiology. From Cell to Bedside, 3rd Edition.. W.B. Saunders Company, Philadelphia, pp. 315–320.

Gray, R.A., Jalife, J., 1998. Ventricular fibrillation and atrial fibrillation are two different beasts. Chaos 8, 65–78.

Gray, R.A., Jalife, J., Panfilov, A.V., Baxter, W.T., Cabo, C., Pertsov, A.M., 1995. Non-stationary vortex-like reentrant activity as a mechanism of polymorphic ventricular tachycardia in the isolated rabbit heart. Circulation 91, 2454–2469.

Green, A.E., Adkins, J.E., 1970. Large Elastic Deformations, 2nd Edition. Clarendon Press, Oxford.

Guccione, J.M., Costa, K.D., McCulloch, A.D., 1995. Finite element stress analysis of left ventricular mechanics in the beating dog heart. J. Biomech. 28 (10), 1167–1177.

Gul'Ko, F.B., Petrov, A.A., 1972. Mechanism of the formation of closed pathways of conduction in excitable media. Biofizika 17, 261–270 (in Russian).

Hodgkin, A.L., Huxley, A.F., 1952. A quantitative description of membrane current and its application to conductance and excitation in nerve. J. Physiol. 117, 500–544.

Hunter, P.J., Nash, M.P., Sands, G.B., 1997. Computational electromechanics of the heart. In: Panfilov, A.V., Holden, A.V. (Eds.), Computational Biology of the Heart. Wiley, West Sussex, England, pp. 345–407 (Chapter 12).

Hunter, P.J., McCulloch, A.D., ter Keurs, H.E.D.J., 1998. Modelling the mechanical properties of cardiac muscle. Prog. Biophys. Molec. Biol. 69, 289–331.

Keener, J.P., 1998. Mathematical Physiology of the Heart. Springer, New York.

Kerckhoffs, R.C.P., Bovendeerd, P.H.M., Kotte, J.C.S., Prinzen, F.W., Smits, K., Arts, T., 2003. Homogeneity of cardiac contraction despite physiological asynchrony of depolarization: a model study. Ann. Biomed. Eng. 31, 536–547.

Kogan, B.Y., Karplus, W.J., Billett, B.S., Pang, A.T., Karagueuzian, H.S., Khan, S.S., 1991. The simplified FitzHugh–Nagumo model with action potential duration restitution: effects on 2D wave propagation. Physica D 50, 327–340.

Kohl, P., Ravens, U. (Eds.), 2003. Mechano-electric feedback and cardiac arrhythmias. Prog. Biophys. Molec. Biol. 82 (1–3), 1–266.

Kohl, P., Hunter, P.J., Noble, D., 1999. Stretch-induced changes in heart rate and rhythm: clinical observations, experiments and mathematical models. Prog. Biophys. Molec. Biol. 71 (1), 91–138.

Luo, C., Rudy, Y., 1994. A dynamic model of the cardiac ventricular action potential: I. Simulations of ionic currents and concentration changes. Circ. Res. 74 (6), 1071–1096.

Malvern, L.E., 1969. Introduction to the Mechanics of a Continuous Medium. Prentice-Hall, Inc., Englewood Cliffs, NJ.

Moe, G.K., Reinbolt, W.C., Abildskov, J.A., 1964. A computer model of atrial fibrillation. Am. Heart J. 67, 200–220.

Nash, M.P., Hunter, P.J., 2000. Computational mechanics of the heart: from tissue structure to ventricular function. J. Elasticity 61 (1/3), 113–141.

Noble, D., 1962. A modification of the Hodgkin–Huxley equation applicable to Purkinje fibre action and pacemaker potentials. J. Physiol. 160, 317–352.

Noble, D., Varghese, A., Kohl, P., Noble, P., 1998. Improved guinea-pig ventricular model incorporating diadic space, i_{kr} and i_{ks}, length and tension-dependent processes. Can. J. Cardiol. 14, 123–134.

Panfilov, A.V., 1998. Spiral breakup as a model of ventricular fibrillation. Chaos 8, 57–64.

Panfilov, A.V., 1999a. Three-dimensional organization of electrical turbulence in the heart. Phys. Rev. E 59, R6251–R6254.

Panfilov, A.V., 1999b. Three-dimensional wave propagation in mathematical models of ventricular fibrillation. In: Zipes, D.P., Jalife, J. (Eds.), Cardiac Electrophysiology. From Cell to Bedside, 3rd Edition.. W.B. Saunders Company, Philadelphia, pp. 271–277.

Panfilov, A.V., 2002. Spiral breakup in an array of coupled cells: the role of the intercellular conductance. Phys. Rev. Lett. 88 (11), 118101.1–118101.4.

Panfilov, A.V., Pertsov, A.M., 1981. Spiral waves in active media, reverberator in the FitzHugh–Nagumo model. In: Autowave Processes in Systems with Diffusion (in Russian). Acad. Sci. USSR, Gorky, pp. 77–84.

Panfilov, A.V., Pertsov, A.M., 1984. Vortex ring in three-dimensional active medium in reaction–diffusion system. Doklady AN USSR 274, 1500–1503 (in Russian).

Panfilov, A.V., Pertsov, A.M., 2001. Ventricular fibrillation: evolution of the multiple wavelet hypothesis. Phil. Trans. Roy. Soc. Lond. 359, 1315–1325.

Pertsov, A.M., Davidenko, J.M., Salomonz, R., Baxter, W.T., Jalife, J., 1993. Spiral waves of excitation underlie reentrant activity in isolated cardiac muscle. Circ. Res. 72 (3), 631–650.

Pool, R., 1990. Heart like a wheel. Science 247, 1294–1295.

Sigurdson, W., Ruknudin, A., Sachs, F., 1992. Calcium imaging of mechanically induced fluxes in tissue-cultured chick heart: role of stretch-activated ion channels. Am. J. Physiol. 262, H1110–H1115.

Smaill, B.H., Hunter, P.J., 1991. Structure and function of the diastolic heart: material properties of passive myocardium. In: Glass, L., Hunter, P.J., McCulloch, A.D. (Eds.), Theory of Heart: Biomechanics, Biophysics, and Nonlinear Dynamics of Cardiac Function. Springer, New York, pp. 1–29.

Spencer, A.J.M., 1980. Continuum Mechanics. Longman Group Limited, London.

Usyk, T.P., LeGrice, I.J., McCulloch, A.D., 2002. Computational model of three-dimensional cardiac electro-mechanics. Comput. Visual. Sci. 4, 249–257.

Vetter, F.J., McCulloch, A.D., 2001. Mechanoelectric feedback in a model of the passively inflated left ventricle. Ann. Biomed. Eng. 29, 414–426.

Winfree, A.T., 1989. Electrical instability in cardiac muscle: phase singularities and rotors. J. Theor. Biol. 138, 353–405.

Zykov, V.S., 1987. Simulation of Wave Processes in Excitable Media. Manchester University Press, Manchester.